Simulation of the concomitant process of nucleation-growth-coarsening of Al_2Cu precipitates and its influence on the mechanical behaviour of a 319 foundry aluminum alloy.

Class & Exercice handbook

M. Georges CAILLETAUD, Professeur, MINES ParisTech, Evry, France
M. Patrice CHAPTAL, Responsable R&D, Société Montupet, Laigneville, France
M. Rémi MARTINEZ, Expert Métallurgie, Société Montupet, Laigneville, France

MINES
ParisTech

MONTUPET S.A.

1   Introduction

The hardening created by the precipitation of hardening particles in the matrix starts with the nucleation of coherent solute-rich Guinier-Preston zones (GP zones). If the size of the nucleus is larger than the critical radius of nucleation, the GP zone can grow to become a GP2 zones [1, 2, 3, 4, 5, 6]. The growth of the GP2 particle to a semi-coherent precipitate is driven by the reduction of the oversaturation of the matrix [7, 8, 9, 10, 11, 12, 13, 14, 15, 16]. The coarsening process, which transforms the semi-coherent particle into a non-coherent one is driven by the reduction of the interfacial energy of the particles [17, 13, 18, 19, 20, 15].

The modeling of the evolution of the size of the precipitates is managed by considering three concomitant regimes : nucleation, growth and coarsening. They provide a general rate of evolution to the precipitates in order to determine the evolution of the mean radius $\bar{R}$ of the size distribution of particles. This approach is mainly based on the works of Kampmann, Wagner and Langer (*KWN* approach) [21, 22, 23] and was first carried out by Myhr *et al.* [24] and Deschamps *et al.* [25].

The *KWN* approach gives a solution based on a 1D discretization of the continuous size distribution of precipitates. The control of the flux of particles toward the system is ensured by an equation of continuity. The switch between growth and coarsening is intrinsic to the model. More recently, the same technique was also used by Robson *et al.* [26, 27], Du *et al.* [28] or Martinez*et al.* [29].

This exercise aims to show how important is the multiscale approach when it comes to accurately model the mechanical behaviour of a metal. After a short presentation of the material (part 2) the metallurgical model is shortly presented in part 3. The coupling of the metallurgy to the mechanics is explained in part 4 and 5 while the exercice is in part 6.

2   Material

The material used in this study is a classical secondary 319 foundry aluminum alloy. It is T7 heat treated - 5 h solutionized, water quenched and 3 h artificialy aged. Its composition is given in table 1.

Elements	% Fe	% Si	% Cu	% Zn	% Mg	% Mn	% Ni	% Pb	% Sn	% Ti
% wt.	<0.70	7.0-8.5	2.8-3.5	<0.80	0.25-0.40	0.10-0.60	<0.30	<0.10	<0.10	0.10-0.20

Table 1: Chemical composition of the 319 aluminum alloy [29].

The microstructure of the alloy is mainly composed of a proeutectic α-phase, globular eutectic silicon and iron inter-metallic compounds. The precipitation of θ (Al_2Cu) occurs during the T7 heat treatment and enhances the mechanical properties of the alloy. Figure 1 shows two dark and a bright field micrographs. These micrographs display the precipitation of the alloy after 48 h of aging at 200°C. The three families of θ' precipitates can be seen. Each family is oriented at 90° because of its habit planes being the $\{100\}$ of the matrix. Indeed, the precipitation happens according to the time-temperature dependent kinetics : GP zone $\rightarrow \theta'' \rightarrow \theta' \rightarrow \theta$ (Al_2Cu).

3   Precipitation kinetics model

In the framework of this work, a few assumptions were taken for the sake of the simplicity of the model.

- the transformation sequence during the precipitation process (GP zone $\rightarrow \theta'' \rightarrow \theta' \rightarrow \theta$) was simplified. The three families of particles are not individually distinguished;

- the nucleation process is assumed to be homogeneous rather than heterogeneous;

- the particles are assumed to be spherical;

- despite the fact that the alloy is a multi-component system, only the diffusion of copper is taken into account. Silicon and magnesium are assumed to remain in solid solution in the matrix during all the process;

- the interfacial energy of the particles is assumed to be independant of both the orientation and the coherency of the interface matrix/precipitate.
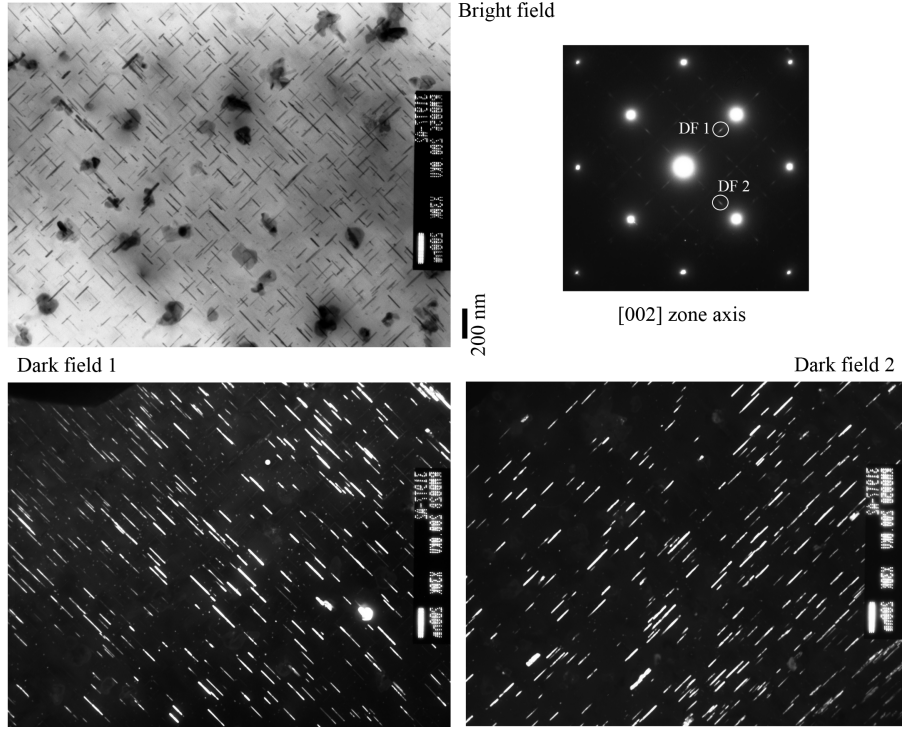
Figure 1: Dark and bright fields TEM micrographs of the θ' precipitation after 48 hours of aging at 200°C [29].

3.1 Thermodynamics of the nucleation process

Thermodynamics allows the variation ΔG of free energy to be determined in a closed volume α if a particle β nucleates during a variation of temperature ΔT. To be stable, this particle has to be larger in size than the critical radius of nucleation $R^\star$, which is defined by equation 1 [30] :

$$R^\star = -\frac{2.\gamma}{\Delta G_V} \tag{1}$$

With γ the interfacial energy, which is assumed to be independant of the boundary orientation, and ΔG_V the variation of free energy per unit volume associated with the formation of the new particle. Considering an incubation period, the time dependent nucleation rate J is given by equation 2 :

$$J = N.Z.\beta^\star.exp\left(\frac{-\Delta G^\star}{k_B.T}\right) exp\left(\frac{-\tau}{t}\right) \tag{2}$$

When an homogeneous nucleation is assumed, N represents the nucleation site density and can be calculated with equation 3 :

$$N = \frac{\mathcal{N}}{V^\alpha} \tag{3}$$

Where $\mathcal{N}$ is Avogadro's number and V^α is the molar volume of the matrix.

In equation 2, the Zeldovich's factor Z converts the equilibrium concentration of the nuclei into the steady state concentration. It is given by the following equation [30] :

$$Z = \frac{V^\alpha.\Delta G_V^2}{8.\pi(\gamma^3.k_B.T)^{1/2}} \tag{4}$$

Where k_B is the Boltzmann's constant and T is the temperature in Kelvin.

The frequency factor $\beta^\star$ (cf. equation 2) is the product of the number of solute atoms in the matrix at the interface nucleus-matrix in contact with that portion, with the jump frequency across the boundary of such solute atoms. The diffusion of the solute atoms is effective across this portion by the jump frequency of solute atoms through the interface. $\beta^\star$ can be calculated with the following equation [30] :

$$\beta^\star = \frac{16.\pi.\gamma^2.D.\bar{C}}{\Delta G_V^2.a^4} \tag{5}$$

Where $D = D_0.exp\left(-\frac{Q}{\mathcal{R}.T}\right)$ is the diffusion coefficient of the solute in the pro-eutectic α-phase, $\bar{C}$ is the mean molar fraction of solute in the matrix and a is the lattice parameter of the matrix.

In equation 2, the free energy $\Delta G^\star$ of a critical particle is the most influential term in the nucleation rate J. $\Delta G^\star$ is determined using the Gibsian approach [30] :

$$\Delta G^\star = \frac{16.\pi\gamma^3}{3.\Delta G_V^2} \tag{6}$$

Finally, the incubation time τ (cf. equation 2) of the nucleation represents in equation 2 the inertia that the closed system has to start the nucleation. It is generally accepted to represent the physics of τ with equation 7 [30] :

$$\tau = \frac{8.k_B.T.\gamma.a^4}{V^\alpha.\Delta G_V^2.D.\bar{C}} \tag{7}$$

3.2 Thermodynamics of the growing process

If one considers a nucleated cluster of molar fraction C_p, embedded in a oversatured matrix, this cluster will grow until the oversaturation of the surrounding matrix becomes non-existent. The growth rate $v_t(R)$ of a particle of radius R is given by equation 8 [31, 20, 25, 24, 30] :

$$v_t(R) = \frac{dR}{dt} = \frac{D}{R}\frac{\bar{C} - C_i}{C_p - C_i} \tag{8}$$

With C_i being the molar fraction in solute at the interface particle/matrix. This concentration is related to the molar fraction of solute in the matrix at equilibrium C_e, through the Gibbs-Thomson equation :

$$C_i = C_e.exp\left(\frac{2.\gamma.V^\beta}{R.\mathcal{R}.T}\right) \tag{9}$$

The solute mass balance allows the value of $\bar{C}$ to be expressed as a function of the volume fraction of particles inside the RVE :

$$\bar{C} = \frac{C_0 - C_p.f_v}{1 - f_v} \tag{10}$$

With C_0 being the initial molar fraction of solute in the matrix and f_v being the volume fraction of particles.

3.3 From growth to coarsening

The control of the transition between growth and coarsening is managed at different levels. The first level consists of a continuous control of the evolution of $\bar{C}$. This can only be done if the mass conservation of the system is strictly respected *via* equation 10. If the system is represented by a continuous size distribution of spherical particles, the volume fraction is given by :

$$f_v = \int_0^\infty \frac{4}{3}.\pi.R^3.\rho(R).dR \tag{11}$$

Where $\rho(R)$ is the continuous size distribution of precipitates.

When the coarsening process starts, the oversaturation of solute in the matrix is close to zero. The critical radius of growth R_c is the radius that has a growth rate of zero.

3.4   Control of the flux of solute in the size space (R)

The conservation of the mass in the system is regulated by the following equation :

$$\frac{d\rho(R)}{dt} = -\frac{dF}{dR} \tag{12}$$

Where F is the flux of particles in the size space (R). Then, equation 12 can be rewritten as :

$$\frac{d\rho(R)}{dt} = -\frac{d\left[\rho(R).v_t(R)\right]}{dR} \tag{13}$$

The discretization of the problem and the use of the finite differences allow the next equation to be written :

$$\frac{\rho_{t+\Delta t}(R) - \rho_t(R)}{\Delta t} = -\left[\frac{\rho(R+\Delta R).v(R+\Delta R) - \rho(R).v_t(R)}{\Delta R}\right]_\theta \tag{14}$$

A fully implicit resolution scheme, with $\theta = t + \Delta t$ is chosen to ensure the stability of the integration. Hence, equation 14 becomes :

$$\frac{\rho_{t+\Delta t}(R) - \rho_t(R)}{\Delta t} = -\left[\frac{\rho_{t+\Delta t}(R+\Delta R).v_t(R+\Delta R) - \rho_{t+\Delta t}(R).v_t(R)}{\Delta R}\right] \tag{15}$$

The equation above can be written in the following general form (eq. 16) :

$$\rho_{t+\Delta t}(R).\,[P] = \rho_{t+\Delta t}(R-\Delta R).\,[G] + \rho_{t+\Delta t}(R+\Delta R)\,[D] + \rho_t(R).\,\left[P^0\right] \tag{16}$$

With $[P]$, $[G]$, $[D]$, and $\left[P^0\right]$ being computation parameters. The use of finite differences allows the adjustment of the scheme as a function of the direction of the fluxes in the size space R. Figure 2 displays, the simplified 1D discrete problem. The use of classes of equivalent size has been used to create a spatial grid along the axis R. Each particle is assumed to belong to a class R, of size ΔR, surrounded by two classes : $R - \Delta R$ and $R + \Delta R$. The discrete problem has then two boundaries that we consider to be R_{min} and R_{max}.

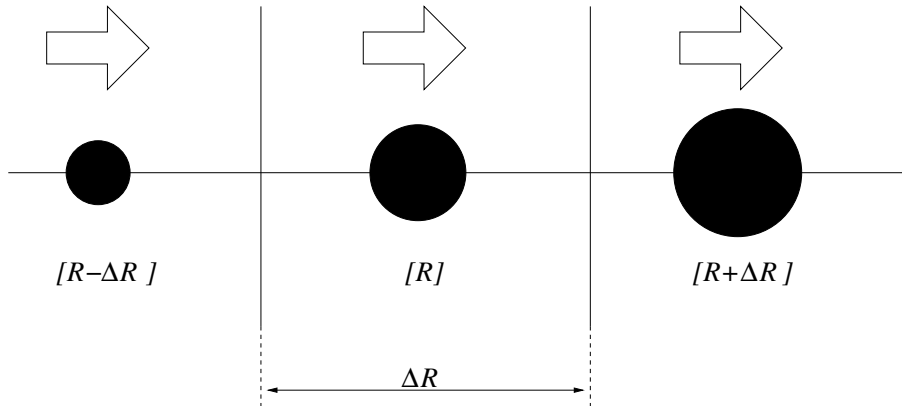

Figure 2:   General scheme of the flux of solute between particles of classes $[R - \Delta R : R + \Delta R]$ [29].

3.5 Tridiagonal matrix

Equation 16 can be expressed by means of a general matricial form, that results from the following notations :

$$\begin{cases} \rho_t(R) & = \rho_n^i \\ \rho_{t+\Delta t}(R) & = \rho_{n+1}^i \\ \rho_{t+\Delta t}(R + \Delta R) & = \rho_{n+1}^{i+1} \\ \rho_{t+\Delta t}(R - \Delta R) & = \rho_{n+1}^{i-1} \end{cases}$$

(17)

So that, equation 16 becomes :

$$\rho_n^i = \rho_{n+1}^{i-1} . \frac{[-G]}{[P^0]} + \rho_{n+1}^i . \frac{[P]}{[P^0]} + \rho_{n+1}^{i+1} . \frac{[-D]}{[P^0]}$$

(18)

Then, the matricial relation appears :

$$\begin{cases} \sum_j \delta_{[i,j]} = \mathbb{1} \\ \sum_j \delta_{[i+1,j]} = M_{[i,j]}^{sup} \\ \sum_j \delta_{[i-1,j]} = M_{[i,j]}^{inf} \end{cases}$$

(19)

Where :

$$M_{[i,j]}^{sup} = \begin{pmatrix} 0 & 1 & 0 & . \\ . & 0 & 1 & 0 \\ . & . & 0 & 1 \\ . & . & . & 0 \end{pmatrix}$$

And :

$$M_{[i,j]}^{inf} = \begin{pmatrix} 0 & . & . & . \\ 1 & 0 & . & . \\ 0 & 1 & 0 & . \\ . & 0 & 1 & 0 \end{pmatrix}$$

The final step is the factorisation of equation 18. The boundary conditions for $R = R_{min}$ and $R = R_{max}$ are automatically taken into account through the computation of the parameters P, G, D and P^0. The matricial form of the general problem becomes :

$$\rho_n = \rho_{n+1} \left(-M_{[i,j]}^{inf} . \frac{[G]}{[P^0]} + \mathbb{1} . \frac{[P]}{[P^0]} - M_{[i,j]}^{sup} . \frac{[D]}{[P^0]} \right)$$

(20)

Which is equivalent to the following generic form :

$$\rho_n^i = \sum_j \mathcal{D}_{[i,j]} \rho_{n+1}^j$$

(21)

Where the matrix $\mathcal{D}_{[i,j]}$ is a tridiagonal matrix defined as :

$$\mathcal{D}_{[i,j]} = \begin{pmatrix} \frac{P[1]}{P[1]^0} & -\frac{R[1]}{P[1]^0} & 0 & 0 \\ -\frac{L[2]}{P[2]^0} & . & . & 0 \\ 0 & . & . & -\frac{R[n-1]}{P[n-1]^0} \\ 0 & 0 & -\frac{L[n]}{P[n]^0} & \frac{P[n]}{P[n]^0} \end{pmatrix}$$

The size distribution at $t + \Delta t$ is directly obtained by multiplying the vector defining the size distribution at time t by the inverse matrix of $\mathcal{D}_{[i,j]}$. Computing $\mathcal{D}_{[i,j]}^{-1}$ is an easy task that could be done numerically by a Lower-Upper method, using a Tri-Diagonal Matrix Algorithm (TDMA) [32, 33].

4 Yield strength modeling

The micro yield stress σ_y of an aluminum alloy is assumed to be close to the yield stress of the dendritic α-phase [25, 34, 35, 36, 37, 38, 39, 40, 41, 42, 43]. It is thus coupled with the evolution of the mean radius of the precipitates and involves the following hardening modes:

- Orowan interaction, σ_{oro};

- Peierls interaction, $\sigma_{lattice}$;

- solid solution hardening, σ_{ss}.

The resulting yield stress writes:

$$\sigma_y = \sigma_{oro} + \sigma_{lattice} + \sigma_{ss} \tag{22}$$

4.1 Determination of the Orowan stress σ_{oro}

Coherent particles are sheared by dislocations, according to the shearing mecanism. Semi-coherent and incoherent particles are bypassed by dislocations, according to Orowan's looping mechanism. In the general case, when the alloy contains shearable and non-shearable particles, the mean obstacle generated by the distribution is:

$$\sigma_{oro} = \frac{\sum_i \rho[i].F[i]}{\sum_i \rho[i]} \tag{23}$$

where $F[i]$ is the obstacle strength.

In the case of shearable particles, $F[i]$ is given by:

$$F[i] = 2.\beta.G.b^2.r[i]/r_{crit} \tag{24}$$

In the case of non-shearable particles, $F[i]$ is independent of $r[i]$ and is given by:

$$F[i] = 2.\beta.G.b^2 \tag{25}$$

with r_{crit} the critical radius for shearing and β a parameter close to 0.5 [25, 37, 44, 45, 35, 36, 43].

4.2 Determination of Peierls stress $\sigma_{lattice}$

Both the nature of the atoms in the lattice and the structure of dislocation core drive the values of $\sigma_{lattice}$ [46, 47, 48, 49]. In FCC crystals, the energy needed to move a dislocation is constant and does not depend on the temperature. According to different studies [50, 25, 40, 36, 37, 42], a value of 10 MPa for $\sigma_{lattice}$ is used here.

4.3 Determination of the solid solution stress σ_{ss}

In aluminium alloys, elements that are in solid solution have an impact on the yield strength value. As they block the glide of the dislocations, these elements rise to solid solution strengthening. The solid solution hardening creted by Cu solid solution atoms σ_{ss} can be expressed as [45]:

$$\sigma_{ss} = k_{Cu}.\bar{C}^{2/3} \tag{26}$$

where k_{Cu} is a scalling factor.

5 Effect of the microstructure on the macroscopic viscoplastic model

The elasto-viscoplastic model used in this section is an extension of a classical unified viscoplastic model for cyclic loading [51, 52]. In a small perturbation framework, the strain is the sum of a thermoelastic strain and an inelastic strain $\varepsilon = \varepsilon^e + \varepsilon^p$. The introduction of isotropic and kinematic hardening leads to the following definition of the elastic domain (equation 27):

$$f(\boldsymbol{\sigma}, \boldsymbol{X}, R) \leq 0 \tag{27}$$

where $\boldsymbol{X}$ is a non linear kinematic hardening variable, R an isotropic hardening non-linear scalar and J the second invariant of the deviatoric effective stress, denoted by $(\boldsymbol{\sigma} - \boldsymbol{X})^d$:

$$J(\boldsymbol{\sigma} - \boldsymbol{X}) = \sqrt{\frac{3}{2}(\boldsymbol{\sigma} - \boldsymbol{X})^d : (\boldsymbol{\sigma} - \boldsymbol{X})^d} \tag{28}$$

The viscoplastic potential Ω of this model is defined by equation 29:

$$\Omega = \frac{K}{n+1}\left(\frac{f}{K}\right)^{n+1} \tag{29}$$

The plastic flow is determined by the normality rule

$$\dot{\boldsymbol{\varepsilon}}^{\boldsymbol{p}} = \frac{\partial \Omega}{\partial \boldsymbol{\sigma}} = \frac{\partial \Omega}{\partial f}\frac{\partial f}{\partial \boldsymbol{\sigma}} = \dot{p}\boldsymbol{n} \tag{30}$$

where $\dot{p}$ is nothing but the cumulated viscoplastic strain rate (equation 31):

$$\dot{p} = \sqrt{\frac{2}{3}\dot{\boldsymbol{\varepsilon}}^{\boldsymbol{p}} : \dot{\boldsymbol{\varepsilon}}^{\boldsymbol{p}}} = \left\langle \frac{f(\boldsymbol{\sigma}, \boldsymbol{X}, R)}{K} \right\rangle^n \tag{31}$$

Two state variables are defined, $\boldsymbol{\alpha}$ for the kinematic hardening and q for the isotropic hardening:

$$\dot{\boldsymbol{\alpha}} = \dot{\boldsymbol{\varepsilon}}^{\boldsymbol{p}} - \frac{3D}{2C}\boldsymbol{X}\dot{p} \tag{32}$$

$$\dot{q} = (1 - bq)\,\dot{p} \tag{33}$$

Hence, the hardening variables could be deduced:

$$\boldsymbol{X} = \frac{2}{3}C\boldsymbol{\alpha} \tag{34}$$

$$R = bQq \tag{35}$$

The advanced versions of this type of model use to introduce several X's. For the sake of CPU efficiency, we restrict ourselves to two X's only. In such a case, the simplified shape of the model for pure tension writes:

$$\sigma = \sigma_y + K\,(\dot{\varepsilon}^p)^{\frac{1}{n}} + Q\left(1 - e^{-b\varepsilon^p}\right) + \frac{C_1}{D_1}\left(1 - e^{-D_1\varepsilon^p}\right) + \frac{C_2}{D_2}\left(1 - e^{-D_2\varepsilon^p}\right) \tag{36}$$

In the following, the model is seen as a "microstructure informed" expression, whose parameters depend on the output of the metallurgical model. The variable σ_y is the result of the theoretical model computing, at each step of time, the value of the critical radius as a function of (t,T) and coupling it to a micromechanical model. All the parameters are temperature dependent.

6 Results of the precipitation model

6.1 Nucleation

It was mentioned in section 3.1 that the activation energy of nucleation $\Delta G^\star$ is the most influential term affecting the nucleation rate J (*cf.* equation 6). Indeed, the parameter $\Delta G^\star$ depends on the free energy ΔG_V associated with the formation of a particle. Its value can be calculated with an analytical model [24, 25] or can be computed with the help of a thermodynamics software [28, 29]. The method used in this work results from a computation performed with the software Thermocalc® and the database TTAL7. The driving force ΔG_V is calculated at different temperatures as a function of the mean molar fraction of solute in the matrix $\bar{C}$ (cf. figure 3). The system considered for the computation is composed of 7 wt.% of Si and 0.3 wt.% of Mg. The fraction of Cu varies from 0.005 wt.% to 3.8 wt.%. The phases Al and Si were allowed to transform while the phases Al_2Cu and $Al_5Cu_2Mg_8Si_6$ were dormant. Using such a mapping enables the model to adapt its own value of ΔG_V as a function of the temperature and $\bar{C}$.
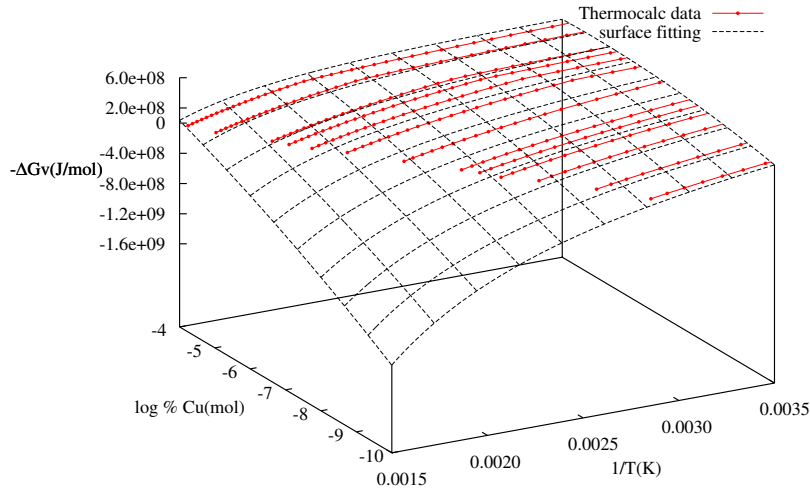

Figure 3: Fitting of the surface generated by Thermocalc to compute ΔG_V as a function of the temperature and the mean molar fraction of solute in the matrix [29].

6.2 Growth and coarsening

The two temperatures used to model growth and coarsening are illustrated in figure 4. A water quench followed by a maturation and two agings at 250°C and 300°C are used to model the T7 thermal treatment.

Figure 5 displays the evolution of the mean radius, the critical radius of growth, the measured radius and the mean radius computed with the *LSW method* [53] as a function of time for the temperatures cited above. Table 2 summarizes the measured and modeled values.

During the quenching process, the main radius $\bar{R}$ decreases during the time that the nucleation rate is accelerating (cf. figure 5). The apparition of the first peak of nucleation occurs at the end of the quenching process and the creation of small particles leads to a drop in the evolution of $\bar{R}$. During the maturation at 23°C, the value of the main radius is steady at 1.8 nm.

When the aging process starts, a second peak of nucleation occurs and leads to a significant drop on the value of $\bar{R}$ because of the important amount of small nucleated particles. In addition, it also can be noticed on figure 5 that the critical radius of growth R_c has always a lower value than R^*. Indeed, R_c only depends on the growth rate while R^* depends on an energetical criterion. Moreover, during nucleation, stable particles have to have a positive growth rate
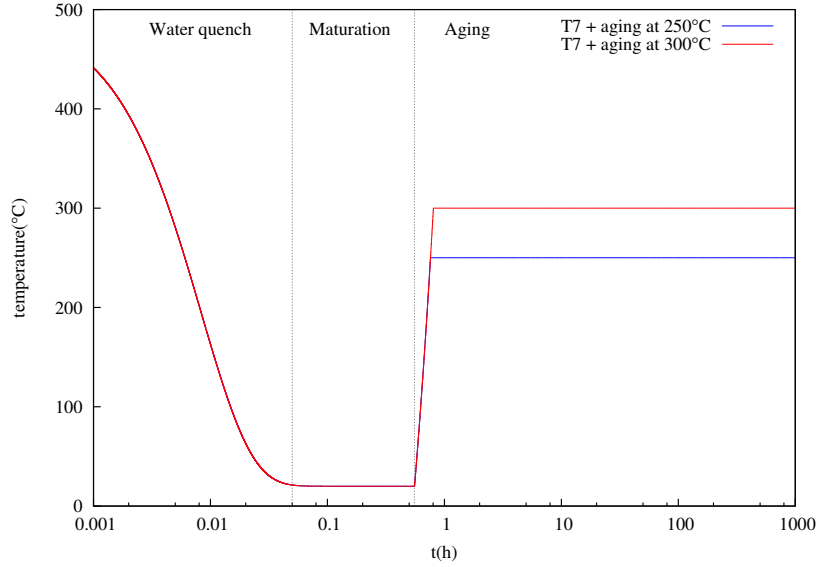
Figure 4: Evolution of the temperature used to model the T7 thermal treatment as a function of time [29].

in order to grow. If the value of R^* was lower than the value of R_c, the nucleated particles would not be stable and would instantaneously be dissolved. In other words, the nucleation would not lead to the generation of a size distribution of particles. After 1000 h of aging at 250°C, the model predicts a mean radius of 34.2 nm while the experimental value is 46.7 nm. At 300°C, the fit between the experimental points and the model is not very accurate until 300 h of aging. Indeed, the almost instantaneous $\theta' \rightarrow \theta$ transformation forces the TEM observations to be in bright field. Since the transformation is not complete, little semi-coherent precipitates remain out of contrast. This leads to their loss during measurements and then to the overestimation of the value of the mean radius. This occurs because bright field observations do not allow a clear distinction between Al_2Cu and other types of smaller particles in the α-phase (*i.e.* agglomerates of Si and lath-shaped Q-phase particles [15, 54, 55, 16]).

Aging	Measured mean radius (nm)	*KWN* mean radius (nm)
T7 + 24 h at 250°C	28.1	24.1
T7 + 96 h at 250°C	28.5	24.1
T7 + 1000 h at 250°C	46.7	34.2
T7 + 48 h at 300°C	59.6	35.3
T7 + 300 h at 300°C	75.0	67.0
T7 + 1000 h at 300°C	85.2	100.2

Table 2: Comparison between the mean radius measured by TEM and the *KWN* simulated mean radius at different stages of aging [29].

The evolution of the volume fraction is consistent with both growth and coarsening theories. While the quench and the maturation do not significantly affect the volume fraction, the peak of nucleation created by the aging quickly changes its value. When the process is mainly dominated by growth, the volume fraction of Al_2Cu particles increases for both temperatures (figure 6). Once all the particles are nucleated and the growing process is over, coarsening takes place and the volume fraction reaches a steady state. At this stage, the volume fraction of Al_2Cu particles is about 3.83% and 3.52% at 250°C and 300°C respectively. Based on a Al-3.2 wt.% Cu 0.819 wt.% Si 0.32 wt.% Mg ternary system, to match the concentration of the matrix at equilibrium at 495°C, a computation with Thermocalc® (*i.e.* at equilibrium)
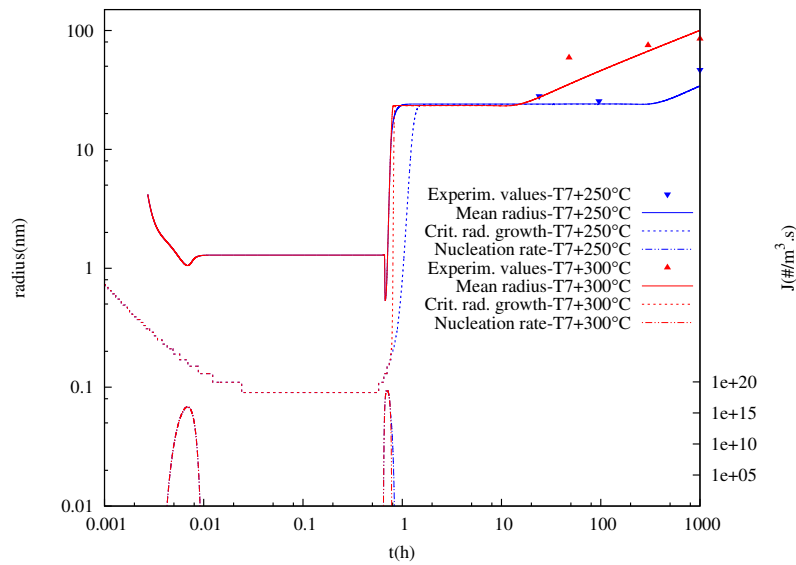
Figure 5: Evolution of the mean radius, the critical radius of growth, the measured radius and the nucleation rate as a function of time at 250°C and 300°C [29].

gives a result of 3.88% at 250°C and 3.59% at 300°C. These values are consistent with the results given by the model.

The evolution of the oversaturation of the matrix as a function of time is also shown in figure 6. During the quenching process the inertia of the nucleation allows the oversaturation to increase as the temperature decreases. At the beginning of the maturation, the oversaturation is at its maximum, and as soon as the precipitation process starts its value decreases to eventually reach zero.

7 Exercise

In this exercise, we ask you to run a multiscale computation in order to improve an innovative heat treatment process. This computation is a chain of local computations in which the heat treatment, the precipitation and the mechanical aspects are disassociated, but are usefull to eachother. Indeed, the thermal computation is used as an input for the precipitation modeling. The latter is performed by means of a local post-processing computation, and its results are strored in each Gauss point of the structure. The plane stress mechanical computation uses the precipitation post-processing results' as an input. The general scheme of the complete chain is presented in figure 7.

The car manufacturer who designed the cylinder head, asked for an improvement of the modeling of the T7 heat treatment in order to minimize the residual stresses. For the sake of simplicity, you are going to model the T7 heat treatment on 1/4 of the fire deck. This is assumed to be representative of the most sensitive area (figure 8). The perfect homogeneity of the solutionizing treatment is assumed. As a consequence we consider only the water quench, from 768K to ambient temperature, followed by 1 hour of maturation at ambient temperature. After the maturation, a high temperature tempering treatment and a final cooling process are applied. In this work, you are asked to investigate the influences of the temperature/time of the tempering, the activation energy of the diffusion and the molar fraction of solute in the precipitates, on the residual stresses after heat treatment.

Each student is going to be part of a group (4 groups of 2 students in total) and each group is going to run 2 chains of computations:
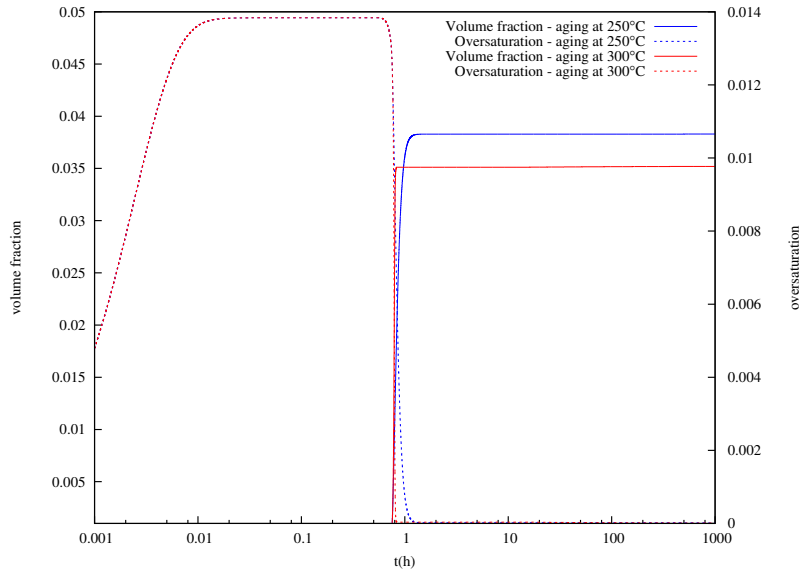**Group 1:**

Figure 6: Evolution of the volume fraction of precipitates and of the oversaturation of the matrix as a function of the time at 250°C and 300°C [29].
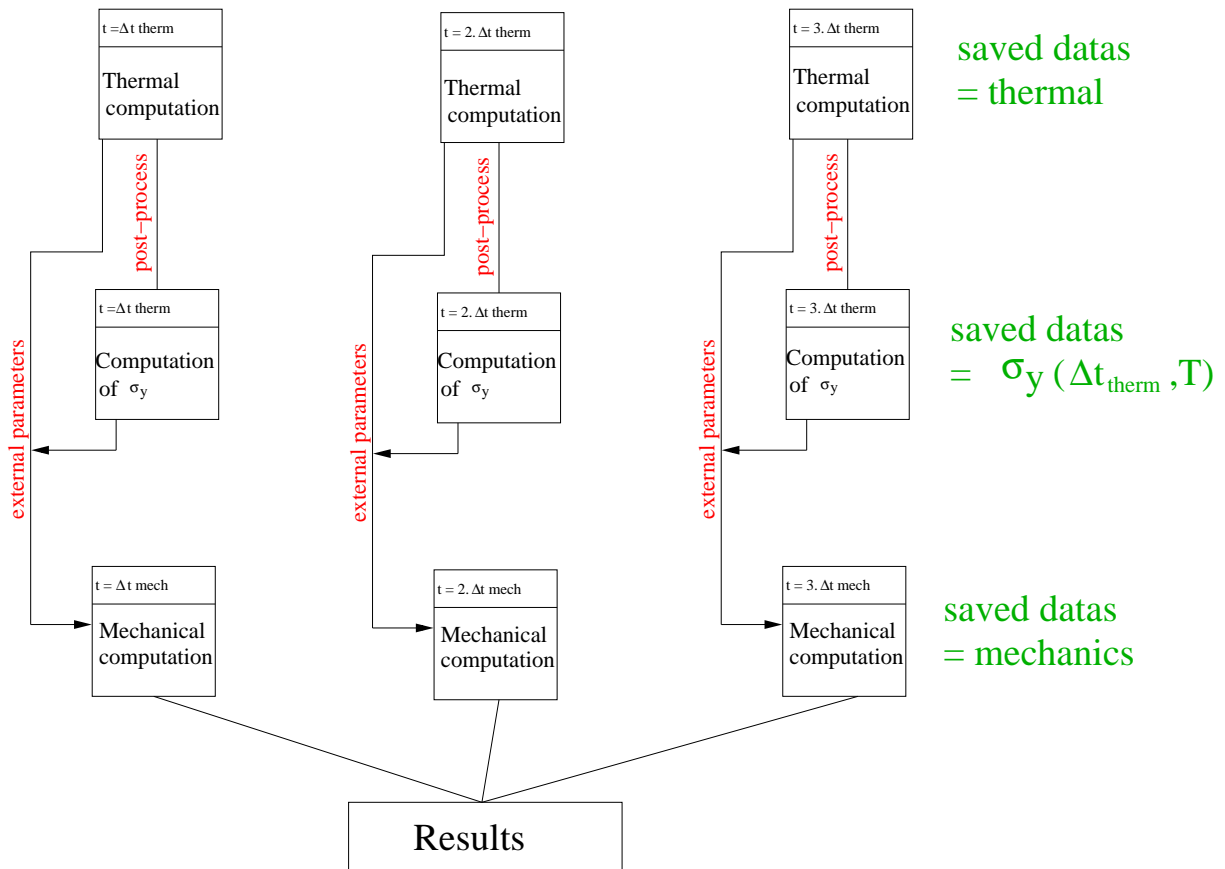

Figure 7: General scheme of the chain of local computation used to model the influence of the parameters on the fire deck [53].
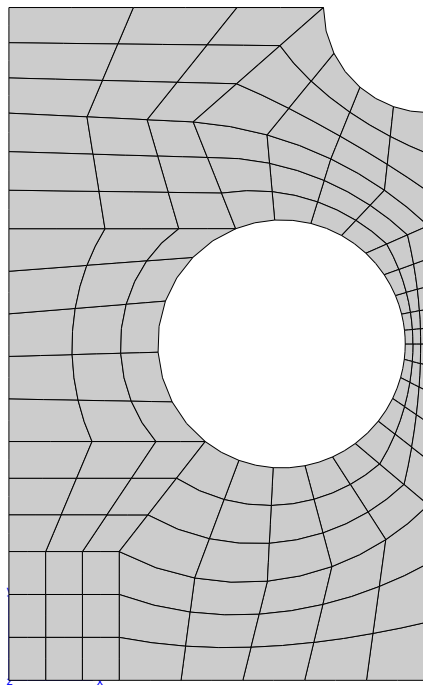
Figure 8: Mesh used to represent the fire deck.

- computation #1: tempering time = 3600s (endTempering = 700s) – tempering temperature = 573K – Q= 120000J/mol – cPrecipitate= 0.334

- computation #2: tempering time = 36000s (endTempering = 33100s) – tempering temperature = 573K – Q= 125000J/mol – cPrecipitate= 1.0

Group 2:

- computation #1: tempering time = 3600s (endTempering = 700s) – tempering temperature = 573K – Q= 125000J/mol – cPrecipitate= 0.334

- computation #2: tempering time = 36000s (endTempering = 33100s) – tempering temperature = 573K – Q= 130000J/mol – cPrecipitate= 1.0

Group 3:

- computation #1: tempering time = 3600s (endTempering = 700s) – tempering temperature = 523K – Q= 120000J/mol – cPrecipitate= 0.334

- computation #2: tempering time = 36000s (endTempering = 33100s) – tempering temperature = 523K – Q= 125000J/mol – cPrecipitate= 1.0

Group 4:

- computation #1: tempering time = 3600s (endTempering = 700s) – tempering temperature = 523K – Q= 125000J/mol – cPrecipitate= 0.334

- computation #2: tempering time = 36000s (endTempering = 33100s) – tempering temperature = 523K – Q= 120000J/mol – cPrecipitate= 1.0

The conclusion of this work is expected to be a detailed report, in which your recommendation concening the best set of parameters are justified.

References

[1] W.A. Johnson and K.E. Mehl. *Trans. Am. Inst. Min. Met. Engrs*, 195:416, 1939.

[2] V. Gerold. Uber die Struktur der bei der Aushärtung einer Aluminium-Kupfer-Legierung auftretenden Zustande. *Z. Metallkunde*, 45:599, 1954.

[3] A. Fontaine, P. Lagarde, A. Naudon, D. Raoux, and D. Spanjaard. EXAFS study on Al-Cu alloys. *Philos. Mag.*, B40:17, 1979.

[4] X. Auvray, P. Georgopoulos, and J.B. Cohen. The structure of GP1 zones in Al-1,7% at. Cu. *Acta Metall.*, 28:1061, 1981.

[5] E. Matsubara and J.B. Cohen. The GP zones in Al-Cu alloys I. *Acta Metall.*, 33:1945, 1985.

[6] M. Karlík, A. Bigot, B. Jouffrey, P. Auger, and S. Belliot. HREM, FIM and tomographic atom probe investigation of Guinier-Preston zones in an Al-1.54 at. % Cu alloy. *Ultramicroscopy*, 98:219, 2004.

[7] M. Avrami. Kinetics of phase change I - General theory. *J. Chem. Phys.*, 7:1103, 1939.

[8] M. Avrami. Kinetics of phase change II - Transformation-time relations for random distribution of nuclei. *J. Chem. Phys.*, 8:212, 1940.

[9] M. Avrami. Kinetics of phase change II - Granulation, phase change and microstructure. *J. Chem. Phys.*, 9:177, 1941.

[10] J.M. Silcock, T.J. Heal, and H.K. Hardy. Structural ageing characteristics of binary aluminium-copper alloys. *J. Inst. Metals*, 82:239, 1953.

[11] G.W. Greenwood. The growth of dispersed precipitates in solution. *Acta Metall.*, 3:243, 1956.

[12] I.M. Lifshitz and V.V. Slyozov. The kinetics of precipitation from supersaturated solid solutions. *J. Phys. Chem. Solids*, 19:35, 1961.

[13] C. Laird and H.I. Aaronson. Mechanisms of formation of θ and dissolution of θ' precipitates in an Al-4% Cu alloy. *Acta Metall.*, 14:171, 1966.

[14] G.C. Weatherly and R.B. Nicholson. An electron microscope investigation of the interfacial structure of semi-coherent precipitates. *Philos. Mag.*, 37B:801, 1968.

[15] D. Ovono-Ovono, I. Guillot, and D. Massinon. The microstructure and precipitation kinetics of a cast aluminium alloy. *Scr. Mater.*, 55:259, 2006.

[16] N. Cherdoudi, J.P. Couzinié, I. Guillot, E. Leroy, B. Barlas, and D. Massinon. Influence of silicon and residual elements on the precipitation of cast aluminium-copper alloy. In *Aluminium alloys: Their physical and mechanical properties. Proceedings of the ICAA 11*, page 969, Weinheim, 2008. Wiley-VCH.

[17] J.D. Boyd and R.B. Nicholson. The coarsening behaviour of θ'' and θ' precipitates in two Al-Cu alloys. *Acta Metall.*, 19:1379, 1971.

[18] D. Vaughan and J.M. Silcock. The orientation and shape of θ precipitates formed in Al-Cu alloy. *Phys. Status Solidi*, 20:725, 1967.

[19] K. Hirano and S. Fujiwara. Impurity diffusion in aluminium. *J. Nucl. Mater.*, 69-70:564, 1978.

[20] L. Ratke and P.W. Voorhees. *Growth and Coarsening-Ripening in Material Processing*. Springer, New York, 2002.

[21] R. Kampmann and R. Wagner. *Decomposition of Alloys: the Early Stages.* Pergamon Press, Oxford, 1984.

[22] Wagner C. Theorie der Alterung von Niederschlägen durch Umlösen (Ostwald-Reifung). *Z. Elektrochem.*, 65:581, 1961.

[23] J.S. Langer and A.J. Schwartz. Kinetics of nucleation in near-critical fluids. *Phys. Rev.*, A21:948, 1980.

[24] O.R. Myhr and O. Grong. Modelling of non-isothermal transformations in alloys containing a particle distribution. *Acta Mater.*, 48:1605, 2000.

[25] A. Deschamps and Y. Bréchet. Influence of predeformation and ageing of an Al-Zn-Mg alloy - II. Modeling of precipitation kinetics and yield stress. *Acta Mater.*, 47:293, 1999.

[26] J.D. Robson. Modelling the overlap of nucleation, growth and coarsening during precipitation. *Acta Mater.*, 52:4669, 2004.

[27] J.D. Robson. A new model for prediction of dispersoid precipitation in aluminium alloys containing zirconium and scandium. *Acta Mater.*, 52:1409, 2004.

[28] Q. Du, W.J. Poole, and M.A. Wells. A mathematical model coupled to calphad to predict precipitation kinetics for multicomponent aluminum alloys. *Acta Mater.*, 60:3830, 2012.

[29] R. Martinez, D. Larouche, G. Cailletaud, I. Guillot, and D. Massinon. Simulation of the concomitant process of nucleation-growth-coarsening of al 2 cu particles in a 319 foundry aluminum alloy. *Model. Simul. Mater. Sc.*, 23(4), 2015.

[30] M. Aaronson, H.I. Enomoto and J.K. Lee. *Mechanisms of diffusional phase transformations in metals and alloys*. CRC Press, Boca Raton, Florida, USA, (2010).

[31] D.A. Porter and K.E. Easterling. *Phase transformations in metals and alloys*. Chapman and Hall, Padstow, Cornwall, 1981.

[32] Moawwad E.A. El-Mikkawy. On the inverse of a general tridiagonal matrix. *Appl. Math. Comput.*, 150:669, 2004.

[33] Moawwad E.A. El-Mikkawy and A. Karawia. Inversion of general tridiagonal matrices. *Appl. Math. Lett.*, 19:712, 2006.

[34] C.A. Gandin, Y. Bréchet, M. Rappaz, G. Canova, M. Ashby, and H. Shercliff. Modelling of solidification and heat treatment for the prediction of yield stress of cast alloys. *Acta Mater.*, 50:901, 2002.

[35] O.R. Myhr, O. Grong, H.G. Fjaer, and C.D. Marioara. Modelling of the microstructure and strength evolution in Al-Mg-Si alloys during multistage thermal processing. *Acta Mater.*, 52:4997, 2004.

[36] A. Simar, Y. Bréchet, B. de Meester, A. Denquin, and T. Pardoen. Sequential modeling of local precipitation, strength and strain hardening in friction stir welds of an aluminum alloy 6005A-T6. *Acta Mater.*, 55:6133, 2007.

[37] C. Gallais, A. Denquin, Y. Bréchet, and G. Lapasset. Precipitation microstructures in an AA6056 aluminium alloy after friction stir welding: Characterisation and modelling. *Mater. Sci. Eng. A*, 496:77, 2008.

[38] C. Genevois, A. Deschamps, A. Denquin, and B. Doisneau-Cottignies. Quantitative investigation of precipitation and mechanical behaviour for AA2024 friction stir welds. *Acta Mater.*, 53:2447, 2005.

[39] C.H. Càceres, J.R. Griffiths, and P. Reiner. The influence of microstructure on the bauschinger effect in an al-si-mg casting alloy. *Acta Mater.*, 44:15, 1995.

[40] S. Esmaeili, D.J. Lloyd, and W.J. Poole. Modeling of precipitation hardening for the naturally aged Al-Mg-Si-Cu alloy AA6111. *Acta Mater.*, 51:3467, 2003.

[41] S. Esmaeili and D.J. Lloyd. Modeling of precipitation hardening in pre-aged AlMgSi(Cu) alloys. *Acta Mater.*, 53:5257, 2005.

[42] G. Fribourg, Y. Bréchet, A. Deschamps, and A. Simar. Microstructure-based modelling of isotropic and kinematic strain hardening in a precipitation-hardened aluminium alloy. *Acta Mater.*, 59:3621, 2011.

[43] J. Zander and R. Sandstrom. One parameter model for strength properties of hardenable aluminium alloys. *Mater. Design*, 29:1540, 2008.

[44] B. Barlas, I. Guillot, G. Cailletaud, M. Clavel, and D. Massinon. Thermomechanical fatigue and aging of cast aluminum alloy: a link between numerical modeling and microstructural approach. In L Rémy and J. Petit, editors, *Journées de printemps de la SF2M*, volume 29, page 75. ESIS publications-Elsevier, 2002.

[45] O.R. Myhr, O. Grong, and S.J. Andersen. Modelling of the age hardening behaviour of Al-Mg-Si alloys. *Acta Mater.*, 48:1605, 2001.

[46] J. Friedel. *Dislocations*. Addison-Wesley Publishing Company Inc., Reading, Massachussets, USA, 1964.

[47] P. Haasen. *Dislocations in Solid-Solution Hardening in f.c.c. metals*. North Holland Publishing Company, Amsterdam, New York, Oxford, 1979.

[48] D. Hull and D.J. Bacon. *Introduction to dislocations*. Butterworth Heinemann, Oxford, 1984.

[49] J.G. Sevillano. *Materials Science and Technology - Plastic deformation and fracture of materials*. VCH Verlagsgesellschaft mbH & VCH Publishers Inc., Weinheim, Germany & New York, USA, 1993.

[50] L.F. Mondolfo. *Aluminium alloys, structure and properties*. Butterworths, London, 1976.

[51] J. Lemaitre and J.L. Chaboche. *Mechanics of Solid Materials.* Cambridge University Press, 1994.

[52] J. Besson, G. Cailletaud, J.L. Chaboche, and S. Forest. *Non-linear mechanics of materials*. Springer, 2009.

[53] R. Martinez, V. Russier, Couzinié, I. Guillot, and G. Cailletaud. Modeling of the influence of coarsening on viscoplastic behaviour of a 319 foundry aluminum alloy. *Mater. Sci. Eng. A*, 559:40, 2013.

[54] D. Ovono-Ovono, I. Guillot, and D. Massinon. Determination of the activation energy in a cast aluminium alloy by TEM and DSC. *J. Alloys Compd.*, 432:241, 2007.

[55] D. Ovono-Ovono, I. Guillot, and D. Massinon. Study on low-cycle fatigue behaviours of the aluminium cast alloys. *J. Alloys Compd.*, 452:425, 2008.